RESEARCH ARTICLE
ATMOSPHERIC PHYSICS

Earth and Planetary Physics
9: 915–924, 2025
doi: 10.26464/epp2025045

Climatology and long-term trends in middle atmospheric temperatures at mid-latitudes observed by the Rayleigh/Sodium Lidar over Hefei, China (32°N, 117°E)

Jian Li[1,2], Wen Yi[1,2*], XiangHui Xue[1,2,3,4*], MaoLin Lu[1,2], JianYuan Wang[1,5,6,7], HaiLun Ye[1,2,7], and TingDi Chen[1,2]

[1]CAS Key Laboratory of Geospace Environment, School of Earth and Space Sciences, University of Science and Technology of China, Hefei 230026, China;

[2]CAS Center for Excellence in Comparative Planetology, Anhui Mengcheng Geophysics National Observation and Research Station, University of Science and Technology of China, Hefei 230026, China;

[3]Hefei National Laboratory, University of Science and Technology of China, Hefei 230026, China;

[4]Collaborate Innovation Center of Astronautical Science and Technology, Harbin 150001, China;

[5]National Key Laboratory of Electromagnetic Environment, China Research Institute of Radiowave Propagation, Qingdao 266107, China;

[6]Yunnan Kunming Electromagnetic Environment National Observation and Research Station, Qujing Kunming 655000, China;

[7]State Key Laboratory of Space Weather, Chinese Academy of Sciences, Beijing 100190, China

Key Points:

- Climatology and long-term trends of the middle atmospheric temperatures are investigated using 12 years of Rayleigh/Sodium Lidar observations.
- The middle atmospheric temperatures mainly show annual oscillations and semi-annual oscillations.
- Middle atmospheric temperatures exhibit a cooling trend across all altitudes, with a positive response to the solar cycle.

Citation: Li, J., Yi, W., Xue, X. H., Lu, M. L., Wang, J. Y., Ye, H. L., and Chen, T. D. (2025). Climatology and long-term trends in middle atmospheric temperatures at mid-latitudes observed by the Rayleigh/Sodium Lidar over Hefei, China (32°N, 117°E). *Earth Planet. Phys.*, *9*(4), 915–924. http://doi.org/10.26464/epp2025045

Abstract: In this study, the climatology and long-term trends of middle atmospheric temperatures at mid-latitudes are investigated using Rayleigh/Sodium lidar observations collected from January 2010 to December 2021 over Hefei, China (32°N, 117°E). The seasonal variations and vertical profiles of lidar-derived temperatures demonstrate strong agreement with temperature measurements from the Microwave Limb Sounder (MLS) instrument on the Earth Observing System (EOS) Aura satellite. In terms of seasonal variation, middle atmospheric temperatures primarily exhibit annual oscillations (AO) and semi-annual oscillations (SAO). Harmonic analysis of the lidar and MLS temperature data reveals close phase alignment for both AO and SAO, with AO amplitudes ranging from 2 to 6 K, and SAO amplitudes from 1 to 4 K. The dependence of temperature on solar forcing was analyzed using the $F_{10.7}$ index as a proxy, showing positive solar response coefficients at all altitudes, with a maximum of 15 ± 1.1 K/100 SFU observed near 42–44 km. After removing the temperature response to solar cycle variations, a cooling trend in mid-latitude temperatures is evident across all altitudes, ranging from 3 to 6 K/decade.

Keywords: rayleigh and sodium lidar; middle atmosphere; temperature; long term trend; annual oscillation; semi-annual oscillation

1. Introduction

The middle atmosphere is a region of Earth's atmosphere ranging in altitude from approximately 15–100 km, and encompassing both the stratosphere and the mesosphere. This region has garnered significant attention due to the presence of various phenomena, including polar stratospheric clouds, noctilucent clouds, stratospheric warming, the mesopause inversion layer, and gravity waves (Witt, 1962; McIntyre, 1982; Steele et al., 1983; Andrews et al., 1987; Meriwether and Gardner, 2000; Fritts and Alexander, 2003). Additionally, the mesosphere is highly sensitive to climate change (Thomas et al., 1989) and is often described as the "miner's canary" for detecting climate change (von Zahn, 2003).

First author: J. Li, lj01511@mail.ustc.edu.cn
Correspondence to: W. Yi, yiwen@ustc.edu.cn
X. H. Xue, xuexh@ustc.edu.cn
Received 29 DEC 2024; Accepted 31 MAR 2025.
First Published online 21 MAY 2025.

It is well established that anthropogenic greenhouse gases, primarily carbon dioxide, have impacted Earth's climate, leading to warming of the troposphere and Earth's surface, and cooling of the middle and upper atmosphere (Angell, 1988, 1991; Trenberth and Olson, 1989; Bailey et al., 1993; Spencer and Christy, 1993;

Chanin, 1993; Christy, 1995; Dunkerton et al., 1998). Additionally, stratospheric ozone depletion has contributed to long-term temperature changes (Fortuin and Kelder, 1996; de F. Forster and Shine, 1997; Ramaswamy et al., 2001). Since Roble and Dickinson (1989) simulated the effects of doubling CO_2 and CH_4 concentrations, observing pronounced cooling in the stratosphere, mesosphere, and thermosphere, significant progress has been made in observing and quantifying long-term temperature trends in the middle atmosphere. For example, Golitsyn et al. (1996) reported cooling trends of 3.5 ± 1 K/decade at 50 km, 8 ± 1.25 K/decade at 60 km, and 5.2 ± 1.3 K/decade at 70 km at mid-latitudes, based on rocket sonde observations. Kishore et al. (2014) used ground-based lidar observations to report cooling rates in the stratosphere and mesosphere of subtropical regions, with values reaching 0.5 to 0.7 K/decade. Satellite data similarly indicate a cooling trend of 0.5 to 1.5 K/decade in the upper stratosphere (Randel et al., 2009). However, due to limitations in data quality and coverage, estimates of middle atmosphere cooling rates vary widely, with values ranging from 0 to 10 K/decade (Beig et al., 2003).

Temperature variability is also associated with the 11-year solar cycle. Analysis of long-term datasets from U.S. rocket sondes, the OHP Rayleigh lidar (1979–2001), and the Stratospheric Sounding Unit (SSU) aboard NOAA satellites has shown that middle atmosphere temperatures respond significantly to the 11-year solar cycle, with notable seasonal and latitudinal variations (Keckhut et al., 2005). Li T et al. (2008) reported inter-annual variability between 15–85 km that responds to the 11-year solar cycle, with a maximum solar cycle response of approximately 1.3 K/100 $F_{10.7}$, based on Hawaii lidar temperature measurements from 1994 to 2007. Fadnavis et al. (2012) analyzed data from the Halogen Occultation Experiment (HALOE) aboard the Upper Atmospheric Research Satellite (UARS) over the period 1992–2005 using a multiple regression model, finding an annual mean temperature response of approximately 0.5 to 1 K/100 SFU. Recently, Qian LY et al. (2019) used the WACCM-X model to simulate middle atmosphere temperatures from 1980 to 2014, finding solar response coefficients that decrease from approximately 3 K/100 SFU near the mesopause to about 1 K/100 SFU in the lower mesosphere. Additionally, long-term temperature variability is influenced by the El Niño-Southern Oscillation (ENSO) and the Quasi-Biennial Oscillation (QBO) (Yulaeva and Wallace, 1994; Baldwin et al., 2001).

In this study, we utilized 12 years of middle atmospheric temperature data from the University of Science and Technology of China (USTC) Rayleigh/Sodium lidar located in Hefei, China, to investigate the climatological trends of the middle atmosphere at mid-latitudes. This rest of this paper is organized as follows: In Section 2, we introduce the USTC Rayleigh/Sodium lidar instruments, along with the data and analysis methods. Section 3 then presents the seasonal variations and long-term temperature trends from 2010 to 2021. Finally, in Section 4, we summarize our conclusions.

2. Data and Method

2.1 USTC Rayleigh and Sodium Lidar

The USTC Rayleigh/Sodium lidar, located on the campus of the University of Science and Technology of China in Hefei, China (32°N, 117°E), consists of two channels: the Rayleigh channel, which detects Rayleigh scattering signals from altitudes of 30–60 km to obtain atmospheric temperature and density with a height resolution of 60 m and a time resolution of 30 s, and the sodium channel, which detects sodium resonance fluorescence scattering signals to obtain sodium densities from 80–105 km. Due to strong background noise from sunlight during the day, which can overload and damage the receiver, the lidar system can only operate on clear nights. Both wideband and narrowband filtering are used in the lidar system to obtain high signal-to-noise ratio (SNR) data under city lights. Table 1 lists the parameters of the lidar system, and further details can be found in Ma J et al. (2019).

In this study, we use temperature data from the Rayleigh channel. The lidar system was established in 2010, and from January 2010 to December 2021, we obtained 620 nights (~5500 hours) of valid data, which is sufficient to study the seasonal variations and oscillations in middle atmosphere temperatures. Figure 1 shows the number of nights with valid datasets for each month and year. It is evident that there is more data in autumn and winter (October–December) compared to spring and summer, which can be attributed to the higher frequency of rain and cloudy conditions in Hefei during the spring and summer months. Additionally, due to equipment maintenance and upgrades, the amount of observational data in 2016 is relatively low.

2.2 EOS Aura/MLS

The Microwave Limb Sounder (MLS) instrument is aboard the EOS Aura spacecraft, which was launched in 2004. It measures atmospheric thermal microwave emissions across five spectral regions, ranging from 115 GHz to 2.5 THz. Temperature retrievals are performed using bands near the O_2 spectral lines at 118 GHz and 239 GHz, as detected by the MLS radiometers (Schwartz et al., 2008). Temperature and geopotential height data from the MLS profiles were selected from a 5° × 20° latitude–longitude grid centered on the location of the USTC Rayleigh lidar. Daily mean temperatures were derived by averaging the satellite measure-

Table 1. System parameters of the USTC Rayleigh/Sodium lidar.

Transmitter	Channel	
Laser	Rayleigh	Sodium
Wavelength (nm)	532	589
Pulse power (mJ)	500	60
Linewidth (cm^{-1})	1 (unseeded)	0.03 (dual grating)
Pulse width (ns)	6	5
Receiver	**Value**	
Telescope	Cassegrain telescope	
Diameter (mm)	1000	
FOV (mrad)	125′	
Chopper rotate rate (rmp)	3000	
Optical filter 1 & 2		
Bandpass (nm)	0.1	

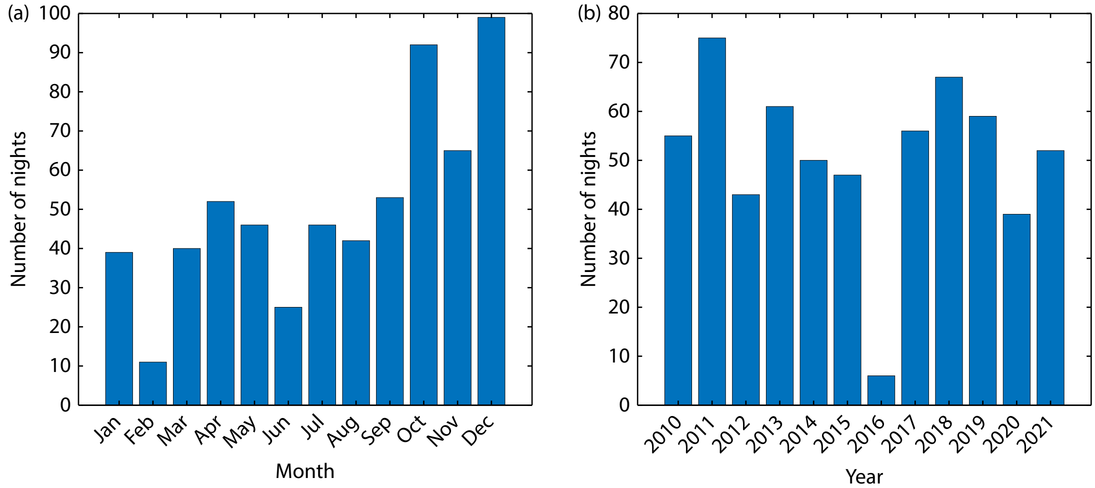

Figure 1. Histogram showing the number of nights with available Rayleigh/Sodium lidar temperature data over Hefei, China, from January 2010 to December 2021. (a) Monthly distribution of observation nights. (b) Annual distribution of observation nights.

ments within this grid.

2.3 Analysis Method

To derive the annual oscillation (AO) and semi-annual oscillation (SAO) from the lidar datasets, we begin by reorganizing the temperature profiles according to their UT day, regardless of the year, to construct a composite dataset for analysis. We then decompose this composite dataset into its mean, along with one-year and half-year periodic components. The uncertainties (error bars) for the AO and SAO amplitudes and phases were estimated based on the variances and covariances derived from least-squares fitting (e.g., Dou XK et al., 2009; Yi W et al., 2021). The decomposition can be expressed as follows:

$$T(t) = T_{\text{mean}} + \sum_{i}^{4} A_i \sin\left(\frac{2\pi i}{365.25}t + \phi_i\right) + \varepsilon(t), \tag{1}$$

where $T(t)$ is temperature measurements, T_{mean} is the mean temperature, $\varepsilon(t)$ is the residual term, and A_i and ϕ_i represent the amplitudes and phases, respectively. The four components in the equation represent the AO, SAO, terannual oscillation (TAO), and quarter oscillation (QAO), respectively.

3. Results

3.1 Temperatures Observed by USTC Rayleigh/Sodium Lidar

Figure 2 shows the composite variation in hourly median nighttime temperature across four different seasons. The observations cover the nighttime period from 8 to 12 hours, with more samples collected in autumn and winter due to the longer nights during these seasons. All profiles exhibit a consistent temperature variation with altitude: temperatures initially increase, reaching a maximum around the stratopause at approximately 50 km, then decrease above this level. In general, temperatures in the middle atmosphere are higher during the spring and summer months compared to the fall and winter seasons.

Figure 3 shows the composite monthly median of the nightly median temperature observed by lidar and MLS. Overall, the temperatures observed by the lidar and those measured by MLS are in good agreement. Both datasets exhibit their maximum near an altitude of 50 km, consistent with the pattern shown in Figure 2. Additionally, both the lidar and MLS observations indicate that the temperature near 50 km reaches maximum values of 269 K (lidar) and 268 K (MLS) in May, and is relatively lower around November, with minimum values of 262 K (lidar) and 258 K (MLS). The temperatures observed by the lidar are slightly higher than those measured by MLS, which may be due to differences in the measurement methods used by ground-based and space-based instruments (e.g., Siva Kumar et al., 2003; Keckhut et al., 2011).

Figure 4 shows the vertical profiles of median temperature derived from long-term lidar and MLS datasets, demonstrating overall good agreement. Both profiles exhibit a characteristic increase in temperature, peaking near 48 km, followed by a decrease above 48 km. This suggests an average stratopause altitude of approximately 48 km in the Hefei region, with a stratopause temperature around 260 K, consistent with the findings of Schöch et al. (2008). However, lidar temperatures are consistently slightly higher than those observed by MLS. At most altitudes, the temperature difference remains within 5 K, although it increases above 55 km, reaching up to 10 K. This discrepancy is likely due to lower signal-to-noise ratios at the edges of the detection range.

Figures 5a and 5b show the characteristics of stratopause altitudes and seasonal variations observed by the lidar and MLS. The altitude of the stratopause varies between 46 and 52 km throughout the year. Compared to the stratopause altitude observed by MLS, the variation in stratopause altitude observed by the lidar is noticeably larger. Stratopause temperatures also show significant variability, ranging from approximately 260 to 272 K. These results are consistent with the observations reported by Guharay et al. (2009). The stratopause temperatures observed by the lidar exhibit a similar variation pattern to those observed by MLS, although the lidar-derived stratopause temperatures are consistently higher than those from MLS. No clear SAO feature was observed at the stratopause altitude. However, a distinct SAO pattern is evident in both the lidar and MLS temperature observations at the

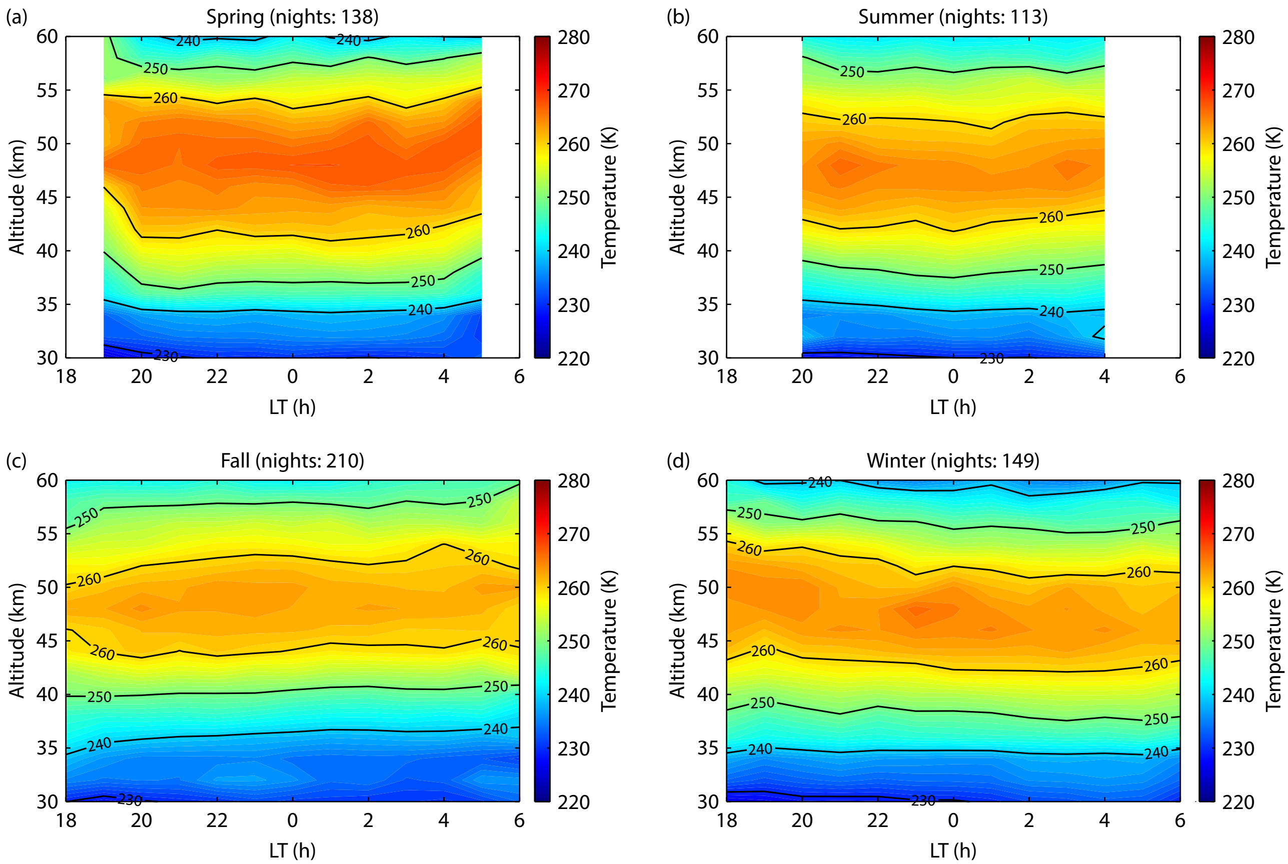

Figure 2. Lidar-observed nighttime hourly median temperature composite over the altitude range 30–60 km in (a) spring, (b) summer, (c) fall and (d) winter. The numbers of nights on different seasons are noted in the figures.

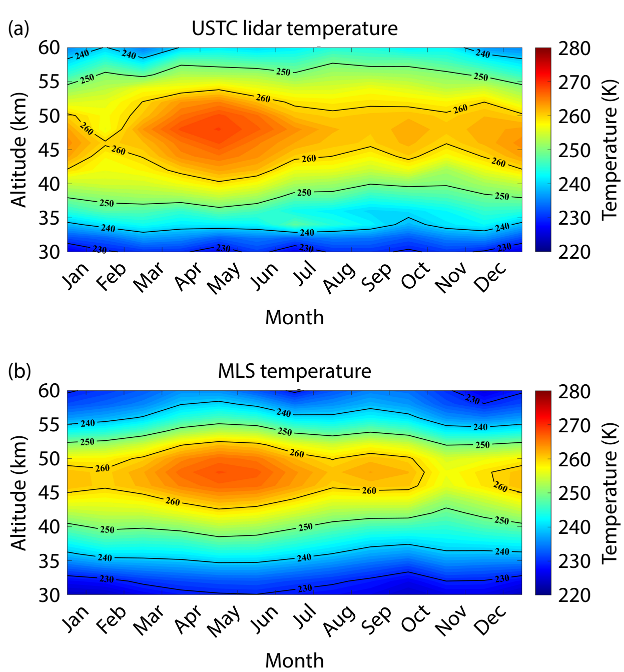

Figure 3. Composite of monthly median temperature from 2010 to 2021 observed by lidar (a) and MLS (b) over the altitude range 30–60 km.

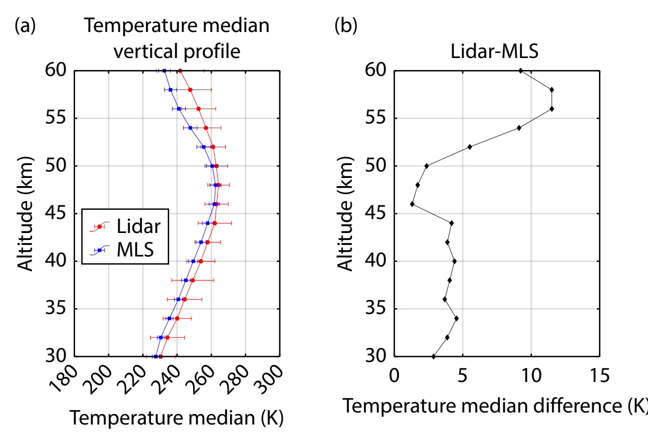

Figure 4. (a) Vertical profiles of the median temperature from lidar (red line) and MLS (blue line) over the altitude range 30–60 km, and (b) the median temperature differences between lidar and MLS.

stratopause, with minima occurring in winter and summer, and maxima in spring and fall.

3.2 Seasonal Variations of Middle Atmospheric Temperatures Observed by Rayleigh Lidar

To investigate the seasonal variation of middle atmospheric

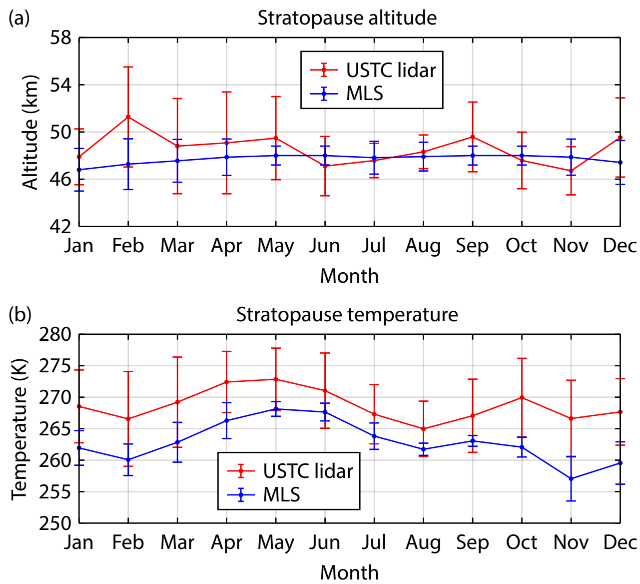

Figure 5. Seasonal variations in the composite monthly mean (a) stratopause altitude and (b) stratopause temperature, as observed by the lidar (red line) and MLS (blue line). The vertical bars represent monthly standard deviations.

temperatures over Hefei at lower mid-latitudes, we calculated the amplitudes and phases of long-period oscillations, namely the AO, SAO, TAO, and QAO, derived using Equation (1). The fitted temperature time series at altitudes of 36 km, 48 km, and 54 km are presented in Figure 6 to demonstrate the quality of the fit.

Figure 7 presents the amplitudes and phases of the AO and SAO as derived from the lidar (red lines) and MLS (blue lines) datasets. Below 40 km, the AO amplitude observed by the lidar is slightly larger than that observed by MLS; however, above 40 km, the reverse is true. The SAO amplitudes observed by the lidar are consistently higher than those observed by MLS, which may result from aliasing effects caused by the diurnal tide, as the subpeak of the diurnal tide temperature occurs at midlatitudes (Forbes, 1995).

Figures 7b and 7d show the phases of the AO and SAO for the lidar and MLS datasets, respectively. The AO phases from both datasets demonstrate strong consistency, with maximum amplitudes appearing in winter and a downward phase trend with increased altitude. In contrast, the SAO phases show good agreement between the lidar and MLS above 45 km, with peak amplitudes in spring and autumn and an upward phase trend above 46 km. Below 45 km, the phase difference between the two gradually decreases, reaching a maximum difference of approximately two months. The AO and SAO are the primary seasonal oscillations in mid-latitude stratospheric temperatures, consistent with the characteristics identified by Xu JY et al. (2007) using TIMED/SABER data to extract zonal mean temperatures in the Northern Hemisphere stratosphere.

3.3 Long Term Temperature Trends Observed by USTC Rayleigh Lidar

To investigate the long-term changes in middle atmospheric temperatures observed by the lidar, we calculated the annual

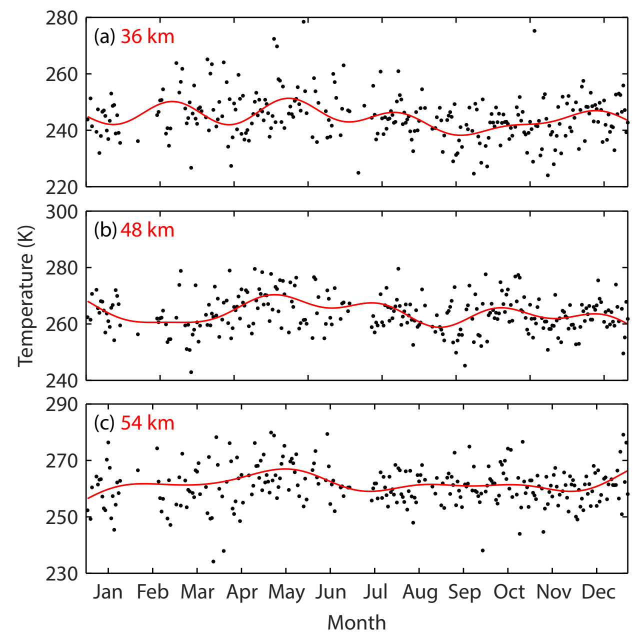

Figure 6. Scatterplot of the composite temperature observed by USTC lidar as a function of the day of the year at three different altitudes: (a) 36 km, (b) 48 km, and (c) 54 km. The red curve represents the harmonic fit derived from Equation (1) using the least squares method.

mean distribution of lidar data from 2010 to 2021, as shown in Figure 8. The red solid line represents the yearly mean $F_{10.7}$ index, which measures the solar radio flux at a wavelength of 10.7 cm. This index, close to the peak of observed solar radio emissions, serves as an indicator of solar activity intensity (Tapping, 2013). The annual mean temperatures observed by the lidar were higher before 2015, reaching a maximum around 2013, and lower after 2017, which aligns with variations in the $F_{10.7}$ index. This suggests that the long-term lidar temperature observations may be influenced by the solar cycle, as it is expected that the middle atmosphere would respond to heating due to ozone absorption of solar ultraviolet radiation, which varies throughout the solar cycle (Li T et al., 2008; Hall et al., 2012).

To further investigate the long-term variation in the lidar-observed temperatures, we used the residual term $\varepsilon(t)$ obtained from Equation (1), which helps to remove the seasonal variations of temperatures. Figure 9a shows the residual temperatures at an altitude of 50 km from 2010 to 2021. A clear cooling trend can be observed in the figure. However, these simple trends may be misleading, as the measurements could be influenced by the solar cycle. If the solar cycle signals are not properly and fully separated, the derived temperature trends in the middle atmosphere may exhibit significant bias (Beig, 2011; Li T et al., 2021). To explore this further, we performed a simple linear regression between the residual temperature data and the corresponding $F_{10.7}$ index. Figure 9b shows that the residual temperatures are positively correlated with the $F_{10.7}$ index, meaning that as the $F_{10.7}$ index increases, the temperature also rises. The response coefficient is approximately 0.05 ± 0.011 K/SFU.

Based on this simple response relationship, the solar-driven

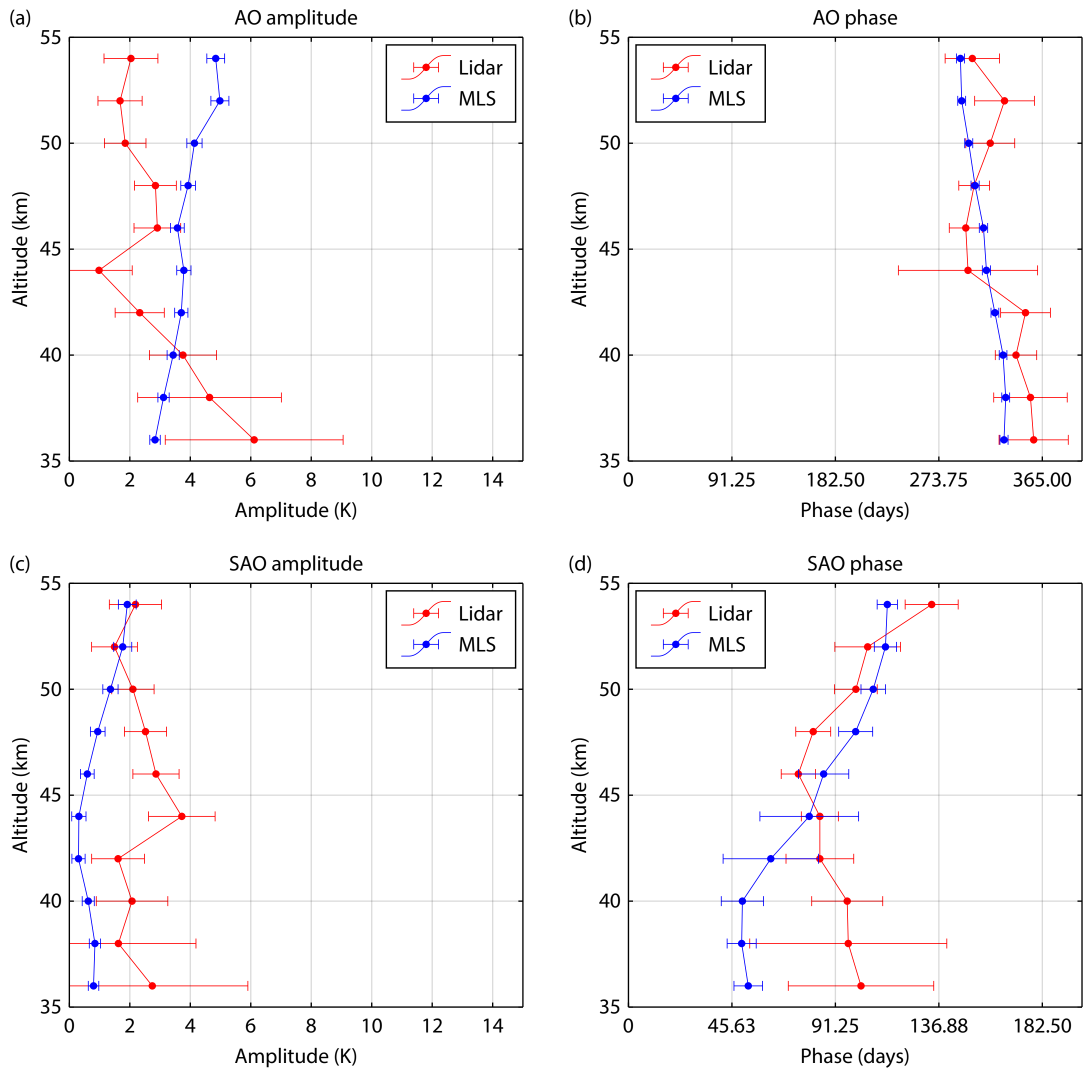

Figure 7. Vertical profiles comparing the AO and SAO amplitudes and phases observed by lidar (red line) and MLS (blue line). (a) AO amplitude, (b) AO phase, (c) SAO amplitude, and (d) SAO phase. The error bars represent the uncertainties associated with the measurements at different altitudes.

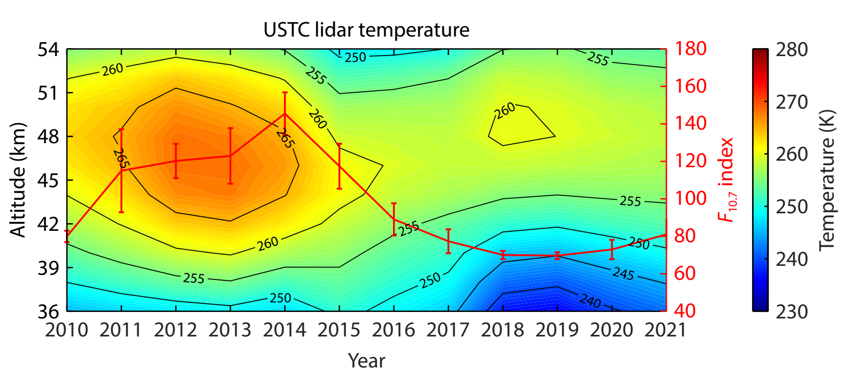

Figure 8. The temperatures observed by the lidar represent the annual mean distribution from 2010 to 2021 between 36–54 km. The red solid line indicates the yearly mean $F_{10.7}$ index, corresponding to the right axis.

temperature sequence is derived from the $F_{10.7}$ flux and subtracted from the residual term $\varepsilon(t)$, yielding the residual temperature ε' minus solar influence:

$$\varepsilon' = \varepsilon(t) - (a + b \times F_{10.7}), \tag{2}$$

where a and b are the coefficients of the linear regression. This method is similar to the one used by Hall et al. (2012). The final calculated results are shown in Figure 9c, where the data have been averaged annually to minimize the interference of short-term signals. It is worth noting that the data for 2016 are insufficient

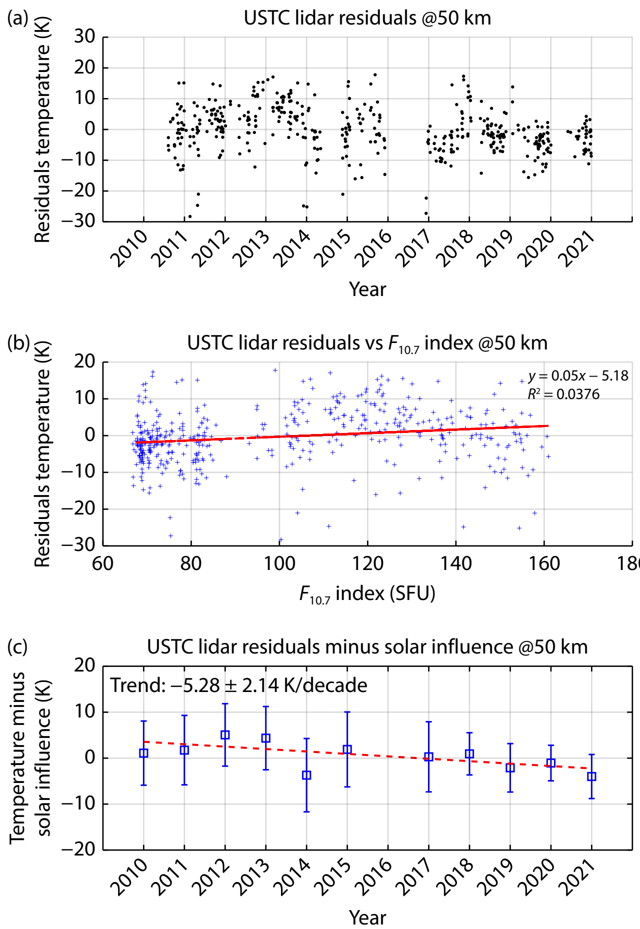

Figure 9. Scatter plot of the residual temperatures at 50 km obtained from Equation (1) (a), scatter plot of the daily mean residual temperature versus the $F_{10.7}$ index (b), and bar chart of the annual mean residual temperature after removing the solar influence, with error bars (c). The red solid and dashed lines represent the linear fits for each respective plot.

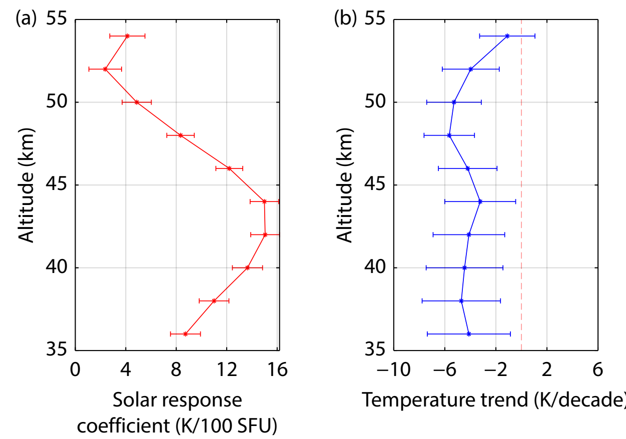

Figure 10. (a) Vertical profile of the solar response parameter and (b) vertical profile of the temperature trend over an altitude range of 36–54 km.

due to equipment maintenance, which may impact the calculation of the annual mean. Therefore, we excluded the 2016 data from the analysis. A linear regression was then applied to determine the long-term temperature variation trend. As shown in Figure 9c, the annual mean temperature residuals at an altitude of 50 km, after removing the solar influence, exhibit a cooling trend, with a cooling rate of 5.28 ± 2.14 K/decade. This result is close to the stratospheric cooling trend observed by Li T et al. (2011) in California (34.4°N) from 1989 to 2010, based on long-term Rayleigh lidar measurements.

Using the aforementioned method, we calculated the solar response coefficients and temperature trends at all altitudes, as illustrated in Figure 10. Note that the units for the solar response coefficients have been converted to K/100 SFU. Figure 10a clearly shows a positive correlation between temperature and the solar cycle in the 36–54 km altitude range. The solar response coefficient increases with altitude and then decreases, reaching a maximum of 15 ± 1.1 K/100 SFU at 42–44 km, and a minimum of 2.4 ± 1.3 K/100 SFU at 52 km. Figure 10b shows a cooling trend in temperature across the 36–54 km altitude range. The cooling trend remains relatively stable, generally ranging between 3 to 6 K/decade. Above 48 km (near the stratopause), the cooling trend shows a significant reduction, with a minimum value of 1.1 ± 2.2 K/decade observed at 54 km.

4. Comparison and Discussion

Table 2 summarizes the the comparison of long-term trends and solar cycle responses ($F_{10.7}$) of middle atmospheric temperatures derived from this study and previous results (Batista et al., 2009; Li

Table 2. Comparison of middle atmospheric temperature trends and solar flux coefficients observed by the different Rayleigh Lidars.[a]

Stations	Time	Altitude	Annual trend	Solar flux coefficient	Reference
Hefei (32°N,117°E)	2010.01–2021.12	36–54 km	from −3 to −6 K/decade	4~15 K/100 SFU	
TMF (34.4°N, 117.7°W)	1989.01–2010.12	35–75 km	from −2 to −4 K/decade	−1~3 K/100 SFU	(Li T et al., 2011)
OHP (43.9°N, 5.7°E)	1981.01–2009.08	35–75 km	from −2 to −3 K/decade	−1~2 K/100 SFU	(Li T et al., 2011)
Gandaki (13.5°N, 79.2°E)	1998–2011	35–65 km	from 0 to −3 K/decade	−1~2 K/100 SFU	(Kishore et al., 2014)
São Josédos Campos (23°S, 46°W)	1993–2006	35–65 km	from −1 to −3 K/decade	/	(Batista et al., 2009)

[a]TMF, the Table Mountain Facility, California; OHP, the Observatoire de Haute Provence, France.

T et al., 2011; Kishore et al., 2014). The comparison highlights a consistent cooling trend in the middle atmosphere across all observations, in agreement with theoretical predictions and model simulations (e.g., Roble and Dickinson, 1989; Akmaev and Fomichev, 1998). While the cooling trends observed by the various lidars differ, the maximum values all exceed 3 K/decade. The varying cooling trends may be attributed to differences in observation locations and the periods covered by the measurements.

Regarding solar cycle responses, the results show significant regional differences. For example, the solar flux coefficients observed in Hefei (4 to 15 K/100 SFU) are considerably higher than those reported at TMF, OHP, and Gandaki (−1 to 3 K/100 SFU), indicating a stronger atmospheric response to solar ultraviolet radiation in Hefei. Increased solar activity enhances ultraviolet radiation, which is absorbed by ozone and molecular oxygen in the stratosphere, triggering heat-releasing photodissociation reactions and localized warming (Brasseur and Simon, 1981; Bednarz et al., 2019).

It is worth noting that the solar cycle signature in stratospheric temperatures is neither globally uniform nor consistent across all altitudes. Horizontal variations have been demonstrated by Labitzke and van Loon (1997), while vertical differences were highlighted by Chanin and Keckhut (1991). These variations can be attributed to the influence of planetary waves and dynamic atmospheric processes, which interact with radiative absorption in complex ways.

The findings underscore the combined impacts of anthropogenic activities and solar forcing on middle atmospheric temperature trends. While CO_2 and ozone dynamics primarily drive the cooling mechanism, the variability in solar flux coefficients across different regions highlights the necessity of conducting regional studies to fully understand the interplay between natural and human-induced factors. Future research should aim to expand spatial and temporal observational datasets and integrate advanced climate models to further unravel these mechanisms and refine our understanding of middle atmospheric processes.

5. Conclusion

.In this study, we analyzed the seasonal variations, solar cycle responses, and long-term trends of middle atmospheric temperatures at mid-latitudes using 11 years of lidar observational data, which were validated through comparisons with MLS data. The following key findings were obtained:

1. The lidar observations were validated by comparison with MLS data, showing high consistency in seasonal variations and vertical distributions, thereby confirming the reliability of the lidar measurements.

2. Harmonic analysis revealed dominant annual oscillations (AO) and semi-annual oscillations (SAO) in middle atmospheric temperatures. AO amplitudes ranged from 2 to 6 K, while SAO amplitudes ranged from 1 to 4 K, reflecting the atmospheric response to seasonal solar radiation changes.

3. A strong positive temperature response to solar activity was observed, with the maximum response occurring near 45 km. Here, an increase of 15 ± 1.1 K per 100 SFU of solar flux was detected.

4. After removing the influence of solar activity, a cooling trend of 3 to 6 K/decade was identified at all altitudes. This trend may be primarily attributed to enhanced radiative cooling from increased CO_2, with ozone playing a secondary role.

Our results highlight the significant impacts of both anthropogenic activities and solar variability on the middle atmosphere. These findings underscore the necessity for sustained long-term observations and advanced modeling efforts to effectively monitor and predict climate changes in this critical region of Earth's atmosphere.

Acknowledgments

This work is supported by the National Natural Science Foundation of China (Grant 42125402, 42174183 and 42304165); the National Key Technologies R&D Program of China (Grant 2022YFF0503703); the B-type Strategic Priority Program of CAS (Grant XDB0780000); the Chinese Meridian Project; the Fundamental Research Funds for the Central Universities; the Joint Open Fund of Mengcheng National Geophysical Observatory (MENGO-202406, MENGO-202407); the National Natural Science Foundation of China (NSFC) Distinguished Overseas Young Talents Program, Basic Research Project of the National Key Laboratory of Deep Space Exploration (NKLDSE2023A002), the Pre-research project on Civil Aerospace Technologies No. D010305 and D010301 funded by China National Space Administration (CNSA). This research was supported by the International Space Science Institute (ISSI) in Bern, through ISSI International Team project #23–580 “Meteors and phenomena at the boundary between Earth’s atmosphere and outer space”. Project is also Supported by the Specialized Research Fund for State Key Laboratory of Solar Activity and Space Weathe.

Data Availability Statement

The Heifei USTC Rayleigh/Sodium Lidar lidar data, YQT lidar data can be downloaded from the Chinese Meridian Project website (https://data2.meridianproject.ac.cn/). Aura/MLS data are available from http://disc.sci.gsfc.nasa.gov/Aura/data-holdings/MLS. The $F_{10.7}$ indices are downloaded from the Center for Space Standards and Innovation (http:// www.celestrak.com/SpaceData/).

References

Akmaev, R. A., and Fomichev, V. I. (1998). Cooling of the mesosphere and lower thermosphere due to doubling of CO_2. *Ann. Geophys.*, *16*(11), 1501–1512. https://doi.org/10.1007/s00585-998-1501-z

Andrews, D. G., Holton, J. R., and Leovy, C. B. (1987). *Middle Atmosphere Dynamics*. Orlando: Academic Press Inc.

Angell, J. K. (1988). Variations and trends in tropospheric and stratospheric global temperatures, 1958-87. *J. Climate*, *1*(12), 1296–1313. https://doi.org/10.1175/1520-0442(1988)001<1296:VATITA>2.0.CO;2

Angell, J. K. (1991). Changes in tropospheric and stratospheric global temperatures, 1958–1988. *Dev. Atmos. Sci.*, *19*, 231–247. https://doi.org/10.1016/B978-0-444-88351-3.50022-2

Bailey, M. J., O'Neill, A., and Pope, V. D. (1993). Stratospheric analyses produced by the United Kingdom Meteorological Office. *J. Appl. Meteor. Climatol.*, *32*(9), 1472–1483. https://doi.org/10.1175/1520-0450(1993)032<1472:SAPBTU>2.0.CO;2

Baldwin, M. P., Gray, L. J., Dunkerton, T. J., Hamilton, K., Haynes, P. H., Randel, W. J., Holton, J. R., Alexander, M. J., Hirota, I., … Takahashi, M. (2001). The quasi-biennial oscillation. *Rev. Geophys.*, *39*(2), 179–229. https://doi.org/10.1029/

1999RG000073

Batista, P. P., Clemesha, B. R., and Simonich, D. M. (2009). A 14-year monthly climatology and trend in the 35-65km altitude range from Rayleigh Lidar temperature measurements at a low latitude station. *J. Atmos. Sol.-Terr. Phys.*, *71*(13), 1456–1462. https://doi.org/10.1016/j.jastp.2008.03.005

Bednarz, E. M., Maycock, A. C., Braesicke, P., Telford, P. J., Abraham, N. L., and Pyle, J. A. (2019). Separating the role of direct radiative heating and photolysis in modulating the atmospheric response to the amplitude of the 11-year solar cycle forcing. *Atmos. Chem. Phys.*, *19*(15), 9833–9846. https://doi.org/10.5194/acp-19-9833-2019

Beig, G., Keckhut, P., Lowe, R. P., Roble, R. G., Mlynczak, M. G., Scheer, J., Fomichev, V. I., Offermann, D., French, W. J. R., … Fadnavis, S. (2003). Review of mesospheric temperature trends. *Rev. Geophys.*, *41*(4), 1–1-1-41. https://doi.org/10.1029/2002rg000121

Beig, G. (2011). Long-term trends in the temperature of the mesosphere/lower thermosphere region: 2. Solar response. *J. Geophys. Res.: Space Phys.*, *116*(A2), A00H12. https://doi.org/10.1029/2011JA016766

Brasseur, G., and Simon, P. C. (1981). Stratospheric chemical and thermal response to long-term variability in solar UV irradiance. *J. Geophys. Res.: Oceans*, *86*(C8), 7343–7362. https://doi.org/10.1029/JC086iC08p07343

Chanin, M. L., and Keckhut, P. (1991). Influence on the middle atmosphere of the 27-day and 11-year solar cycles: Radiative and/or dynamical forcing?. *J. Geoelectr.*, *43*(2), 647–655. https://doi.org/10.5636/jgg.43.Supplement2_647

Chanin, M. L. (1993). Long term trend in the middle atmosphere temperature. In: M. L. Chanin (Ed.), *The Role of the Stratosphere in Global Change*. (Vol. 8, pp. 301-317). Berlin, Heidelberg: Springer. https://doi.org/10.1007/978-3-642-78306-7_14

Christy, J. R. (1995). Temperature above the surface layer. *Climatic Change*, *31*(2), 455–474. https://doi.org/10.1007/BF01095157

de F. Forster, P. M., and Shine, K. P. (1997). Radiative forcing and temperature trends from stratospheric ozone changes. *J. Geophys. Res.: Atmos.*, *102*(D9), 10841–10855. https://doi.org/10.1029/96JD03510

Dou, X. K., Li, T., Xu, J. Y., Liu, H. L., Xue, X. H., Wang, S., Leblanc, T., McDermid, I. S., Hauchecorne, A., … Russell III, J. M. (2009). Seasonal oscillations of middle atmosphere temperature observed by Rayleigh lidars and their comparisons with TIMED/SABER observations. *J. Geophys. Res.: Atmos.*, *114*(D20), D20103. https://doi.org/10.1029/2008JD011654

Dunkerton, T. J., Delisi, D. P., and Baldwin, M. P. (1998). Middle atmosphere cooling trend in historical rocketsonde data. *Geophys. Res. Lett.*, *25*(17), 3371–3374. https://doi.org/10.1029/98GL02385

Fadnavis, S., Beig, G., and Chakraborti, T. (2012). Decadal solar signal in ozone and temperature through the mesosphere of Northern tropics. *J. Atmos. Sol.-Terr. Phys.*, *78-79*, 2-7. https://doi.org/10.1016/j.jastp.2010.09.035

Forbes, J. M. (1995). Tidal and planetary waves. In R. M. Johnson, et al. (Eds.), *The Upper Mesosphere and Lower Thermosphere: A Review of Experiment and Theory* (Vol. 87, pp. 67-87). Washington: AGU. https://doi.org/10.1029/GM087p0067

Fortuin, J. P. F., and Kelder, H. (1996). Possible links between ozone and temperature profiles. *Geophys. Res. Lett.*, *23*(12), 1517–1520. https://doi.org/10.1029/96GL01235

Fritts, D. C., and Alexander, M. J. (2003). Gravity wave dynamics and effects in the middle atmosphere. *Rev. Geophys.*, *41*(1), 3–1-3-64. https://doi.org/10.1029/2001RG000106

Guharay, A., Nath, D., Pant, P., Pande, B., Russell, J. M., and Pandey, K. (2009). Middle atmospheric thermal structure obtained from Rayleigh lidar and TIMED/SABER observations: A comparative study. Journal of Geophysical Research: Atmospheres, 114(D18). https://doi.org/10.1029/2009jd011963

Golitsyn, G. S., Semenov, A. I., Shefov, N. N., Fishkova, L. M., Lysenko, E. V., and Perov, S. P. (1996). Long-term temperature trends in the middle and upper atmosphere. *Geophys. Res. Lett.*, *23*(14), 1741–1744. https://doi.org/10.1029/96GL01592

Hall, C. M., Dyrland, M. E., Tsutsumi, M., and Mulligan, F. J. (2012). Temperature trends at 90 km over Svalbard, Norway (78°N 16°E), seen in one decade of meteor radar observations. *J. Geophys. Res.: Atmos.*, *117*(D8), D08104. https://doi.org/10.1029/2011jd017028

Keckhut, P., Cagnazzo, C., Chanin, M. L., Claud, C., and Hauchecorne, A. (2005). The 11-year solar-cycle effects on the temperature in the upper-stratosphere and mesosphere: Part I—Assessment of observations. *J. Atmos. Sol.-Terr. Phys.*, *67*(11), 940–947. https://doi.org/10.1016/j.jastp.2005.01.008

Keckhut, P., Randel, W. J., Claud, C., Leblanc, T., Steinbrecht, W., Funatsu, B. M., Bencherif, H., McDermid, I. S., Hauchecorne, A., … Baumgarten, G. (2011). An evaluation of uncertainties in monitoring middle atmosphere temperatures with the ground-based lidar network in support of space observations. *J. Atmos. Sol.-Terr. Phys.*, *73*(5-6), 627–642. https://doi.org/10.1016/j.jastp.2011.01.003

Kishore, P., Venkat Ratnam, M., Velicogna, I., Sivakumar, V., Bencherif, H., Clemesha, B. R., Simonich, D. M., Batista, P. P., and Beig, G. (2014). Long-term trends observed in the middle atmosphere temperatures using ground based LIDARs and satellite borne measurements. *Ann. Geophys.*, *32*(3), 301–317. https://doi.org/10.5194/angeo-32-301-2014

Labitzke, K., and van Loon, H. (1997). The signal of the 11-year sunspot cycle in the upper troposphere-lower stratosphere. *Space Science Reviews*, *80*, 393–410. https://doi.org/10.1023/A:1004907126955

Li, T., Leblanc, T., and McDermid, I. S. (2008). Interannual variations of middle atmospheric temperature as measured by the JPL lidar at Mauna Loa Observatory, Hawaii (19.5°N, 155.6°W). *J. Geophys. Res.: Atmos.*, *113*(D14), D14109. https://doi.org/10.1029/2007jd009764

Li, T., Leblanc, T., McDermid, I. S., Keckhut, P., Hauchecorne, A., and Dou, X. K. (2011). Middle atmosphere temperature trend and solar cycle revealed by long-term Rayleigh lidar observations. *J. Geophys. Res.: Atmos.*, *116*(D4), D00P05. https://doi.org/10.1029/2010jd015275

Li, T., Yue, J., Russell, J. M., and Zhang, X. (2021). Long-term trend and solar cycle in the middle atmosphere temperature revealed from merged HALOE and SABER datasets. *J. Atmos. Sol.-Terr. Phys.*, *212*, 105506. https://doi.org/10.1016/j.jastp.2020.105506

Ma, J., Xue, X. H., Dou, X. K., Chen, T. D., Tang, Y. H., Jia, M. J., Zou, Z. C., Li, T., Fang, X., … Sun, S. J. (2019). Large-scale horizontally enhanced sodium layers coobserved in the midlatitude region of China. *J. Geophys. Res.: Space Phys.*, *124*(9), 7614–7628. https://doi.org/10.1029/2018JA026448

McIntyre, M. E. (1982). How well do we understand the dynamics of stratospheric warmings?. *J. Meteor. Soc. Japan. Ser. II*, *60*(1), 37–65. https://doi.org/10.2151/jmsj1965.60.1_37

Meriwether, J. W., and Gardner, C. S. (2000). A review of the mesosphere inversion layer phenomenon. *J. Geophys. Res.: Atmos.*, *105*(D10), 12405–12416. https://doi.org/10.1029/2000JD900163

Qian, L. Y., Jacobi, C., and McInerney, J. (2019). Trends and solar irradiance effects in the mesosphere. *J. Geophys. Res.: Space Phys.*, *124*(2), 1343–1360. https://doi.org/10.1029/2018ja026367

Ramaswamy, V., Chanin, M. L., Angell, J., Barnett, J., Gaffen, D., Gelman, M., Keckhut, P., Koshelkov, Y., Labitzke, K., … Swinbank, R. (2001). Stratospheric temperature trends: Observations and model simulations. *Rev. Geophys.*, *39*(1), 71–122. https://doi.org/10.1029/1999rg000065

Randel, W. J., Shine, K. P., Austin, J., Barnett, J., Claud, C., Gillett, N. P., Keckhut, P., Langematz, U., Lin, R., … Yoden, S. (2009). An update of observed stratospheric temperature trends. *J. Geophys. Res.: Atmos.*, *114*(D2), D02107. https://doi.org/10.1029/2008jd010421

Roble, R. G., and Dickinson, R. E. (1989). How will changes in carbon dioxide and methane modify the mean structure of the mesosphere and thermosphere?. *Geophys. Res. Lett.*, *16*(12), 1441–1444. https://doi.org/10.1029/GL016i012p01441

Schöch, A., Baumgarten, G., and Fiedler, J. (2008). Polar middle atmosphere temperature climatology from Rayleigh lidar measurements at ALOMAR (69°N). *Ann. Geophys.*, *26*(7), 1681–1698. https://doi.org/10.5194/angeo-26-1681-2008

Schwartz, M. J., Lambert, A., Manney, G. L., Read, W. G., Livesey, N. J., Froidevaux, L., Ao, C. O., Bernath, P. F., Boone, C. D., ... Wu, D. L. (2008). Validation of the Aura Microwave Limb Sounder temperature and geopotential height measurements. *J. Geophys. Res.: Atmos.*, *113*(D15), D15S11. https://doi.org/10.1029/2007jd008783

Siva Kumar, V., Rao, P. B., and Krishnaiah, M. (2003). Lidar measurements of stratosphere-mesosphere thermal structure at a low latitude: Comparison with satellite data and models. *J. Geophys. Res.: Atmos.*, *108*(D11), 4342.

https://doi.org/10.1029/2002JD003029

Spencer, R. W., and Christy, J. R. (1993). Precision lower stratospheric temperature monitoring with the MSU: Technique, validation, and results 1979–1991. *J. Climate*, *6*(6), 1194–1204. https://doi.org/10.1175/1520-0442(1993)006<1194:PLSTMW>2.0.CO;2

Steele, H. M., Hamill, P., McCormick, M. P., and Swissler, T. J. (1983). The formation of polar stratospheric clouds. *J. Atmos. Sci.*, *40*(8), 2055–2068. https://doi.org/10.1175/1520-0469(1983)040<2055:TFOPSC>2.0.CO;2

Tapping, K. F. (2013). The 10.7 cm solar radio flux ($F_{10.7}$). *Space Wea.*, *11*(7), 394–406. https://doi.org/10.1002/swe.20064

Thomas, G. E., Olivero, J. J., Jensen, E. J., Schroeder, W., and Toon, O. B. (1989). Relation between increasing methane and the presence of ice clouds at the mesopause. *Nature*, *338*(6215), 490–492. https://doi.org/10.1038/338490a0

Trenberth, K. E., and Olson, J. G. (1989). Temperature trends at the South Pole and McMurdo Sound. *J. Climate*, *2*(10), 1196–1206. https://doi.org/10.1175/1520-0442(1989)002<1196:TTATSP>2.0.CO;2

von Zahn, U. (2003). Are noctilucent clouds a "Miner's Canary" for global change?. *Eos, Trans. Amer. Geophys. Union*, *84*(28), 261–264. https://doi.org/10.1029/2003EO280001

Witt, G. (1962). Height, structure and displacements of noctilucent clouds. *Tellus A*, *14*(1), 1–18. https://doi.org/10.3402/tellusa.v14i1.9524

Xu, J. Y., Smith, A. K., Yuan, W., Liu, H. L., Wu, Q., Mlynczak, M. G., and Russell, J. M. (2007). Global structure and long-term variations of zonal mean temperature observed by TIMED/SABER. *J. Geophys. Res.: Atmos.*, *112*(D24), D24106. https://doi.org/10.1029/2007jd008546

Yi, W., Xue, X. H., Reid, I. M., Murphy, D. J., Hall, C. M., Tsutsumi, M., Ning, B. Q., Li, G. Z., Yang, G. T., … Dou, X. K. (2021). Climatology of interhemispheric mesopause temperatures using the high-latitude and middle-latitude meteor radars. *J. Geophys. Res.: Atmos.*, *126*(6), e2020JD034301. https://doi.org/10.1029/2020jd034301

Yulaeva, E., and Wallace, J. M. (1994). The signature of ENSO in global temperature and precipitation fields derived from the microwave sounding unit. *J. Climate*, *7*(11), 1719–1736. https://doi.org/10.1175/1520-0442(1994)007<1719:TSOEIG>2.0.CO;2